Influence of $L1_0$ order parameter on Gilbert damping constants for FePd thin films investigated by means of time-resolved magneto-optical Kerr effect

Satoshi Iihama,[1,*] Akimasa Sakuma,[1] Hiroshi Naganuma,[1] Mikihiko Oogane,[1] Shigemi Mizukami,[2] and Yasuo Ando[1]
[1]*Department of Applied Physics, Graduate School of Engineering, Tohoku University, Japan*
[2]*WPI Advanced Institute for Materials Research, Tohoku University, Japan*
(Received 23 August 2016; revised manuscript received 11 October 2016; published 15 November 2016)

We have systematically investigated the Gilbert damping constant α for $L1_0$-FePd films using the time-resolved magneto-optical Kerr effect (TRMOKE). The field angle dependence of TRMOKE signals was measured and analyzed. The field angle dependence of the lifetime of magnetization precession was explained by evaluating extrinsic contributions such as the anisotropy distribution and two-magnon scattering. The crystalline uniaxial perpendicular magnetic anisotropy constant K_u and α values were evaluated for FePd films for various $L1_0$ order parameters S. K_u values of approximately 15 Merg/cm^3 were obtained for films with large-S values (i.e., over 0.8). In addition, α for the low-S film was found to be approximately 0.007 and decreased with increasing S. Smaller values of α (of 0.002–0.004) were obtained for films with S values of approximately 0.6–0.8. Results revealed that FePd films have both large-K_u and small-α values, which is a useful property for low-power magnetization switching while maintaining high thermal stability in spin-transfer-torque magnetoresistive random access memory applications.

DOI: 10.1103/PhysRevB.94.174425

I. INTRODUCTION

Magnetic materials that have large perpendicular magnetic anistropy (PMA) have attracted attention for their application to high-density magnetic recording. To retain magnetization direction despite thermal fluctuation over at least 10 years, the following thermal stability condition must be satisfied, $K_u^{\mathrm{eff}} V / k_{\mathrm{B}} T > 60$, where K_u^{eff}, V, and $k_{\mathrm{B}} T$ are the effective uniaxial PMA constant, volume of the ferromagnet, and thermal energy, respectively. One promising material is $L1_0$-ordered alloy, such as $L1_0$-FePt and FePd, because it exhibits a large crystalline magnetic anisotropy constant K_u, i.e., above 10 Merg/cm^3 [1–3].

In addition to thin films with large PMA values being required, the Gilbert damping constant α has also attracted considerable attention because α determines many parameters that are important for device operation such as switching speed of magnetization, fluctuation noise of magnetization [4], and critical current density of spin-transfer-torque magnetization switching [5]. Materials that have large-K_u and small-α values are desirable for realizing low-power magnetization switching while maintaining high thermal stability in spin-transfer-torque magnetoresistive random access memory (STT-MRAM).

For the above reason, investigation of magnetization dynamics is important when evaluating α. Magnetization dynamics is described by the Landau-Lifshitz-Gilbert (LLG) equation as follows:

$$\frac{d\boldsymbol{m}}{dt} = -\gamma \boldsymbol{m} \times \boldsymbol{H}_{\mathrm{eff}} + \alpha \boldsymbol{m} \times \frac{d\boldsymbol{m}}{dt}, \tag{1}$$

where $\boldsymbol{m}$, γ, $\boldsymbol{H}_{\mathrm{eff}}$, and α are the unit vector of magnetization, gyromagnetic ratio, effective magnetic field vector, and Gilbert damping constant, respectively. The precession frequency of the film with large PMA increases to several tens to hundreds of gigahertz. The all-optical time-resolved magneto-optical Kerr effect (TRMOKE) technique is a good candidate for detecting the fast magnetization dynamics of films with large PMA values.

According to the theory regarding K_u, crystalline PMA energy ΔE can be formulated as follows [6]: $\Delta E \propto \lambda_{\mathrm{SO}}(\mu_L^{\parallel} - \mu_L^{\perp})$, where λ_{SO}, $\mu_L^{\parallel}$, and $\mu_L^{\perp}$ are the spin-orbit coupling constant, and the orbital magnetic moment for the in-plane direction and perpendicular direction, respectively. The large-K_u value of $L1_0$-FePt and FePd may be due to the large λ_{SO} values of Pt or Pd atoms and large differences in orbital magnetic moment. A first-principles calculation of K_u for $L1_0$ ordered alloys indicates that the $L1_0$ order parameter is a significant factor for achieving a large-K_u value [7].

On the other hand, according to the theory regarding α [8–11], α also originates from spin-orbit coupling. There are two contributions to α, which are related to interband and intraband transitions of electron via spin-orbit coupling. The interband contribution is electron-phonon scattering due to changes in the spin-orbit coupling energy during the magnetization precession. This contribution is proportional to the electron scattering rate, i.e., $\alpha^{\mathrm{inter}} \propto 1/\tau_e$, where τ_e is the electron-phonon scattering time. At the same time, the intraband contribution is that the eigenenergy of the electron band is excited by magnetization precession via the spin-orbit interaction; thereafter, the nonequilibrium electron relaxes to the states of the same band. This contribution is proportional to electron scattering time, i.e., $\alpha^{\mathrm{intra}} \propto \tau_e$. The temperature dependence of α investigated by Bhagat *et al.* [12] can be explained as a combination of these two contributions. Note that $1/\tau_e$ will increase in the disordered structure because of the random arrangement of the atoms. Recently, Ma *et al.* reported that α for $L1_0$-FePt film increased with increasing antisite disorder, which is associated with τ_e [13].

Whereas the magnetization dynamics for FePt film with PMA are intensively investigated [13–17], there are few

*s.iihama@aist.go.jp

reports on FePd films. Although the α value of FePt was reported to be very large (i.e., over 0.04), the α value of FePd seems to be smaller than that of FePt. α values for FePd reported in Refs. [14,18] were less than 0.01; however, FePd films of previous reports showed in-plane magnetic anisotropy. In addition, the influence of the $L1_0$ order parameter on α is not yet well understood and has not been investigated for FePd films. Previously, we investigated the magnetization dynamics of $L1_0$-FePd film with PMA [19,20] using a TRMOKE technique; the dynamics depended on the measurement condition and the film quality, which indicates that inhomogeneous extrinsic mechanisms such as anisotropy distribution and two-magnon scattering contributed to the increase in magnetization damping. Therefore, the α value of FePd film with PMA has not yet been clarified. Intrinsic α values and extrinsic contributions such as anisotropy distribution and two-magnon scattering will be separated by performing field-angle-dependent measurements [21].

In this study, we performed a systematic investigation of magnetization dynamics and α values for FePd film using a TRMOKE technique. The field angle dependence of the magnetization dynamics was analyzed in detail. α values that have various $L1_0$ order parameters were evaluated by considering extrinsic contributions such as anisotropy distribution and two-magnon scattering. The evaluated α values are discussed based on the results of first-principles calculation.

II. EXPERIMENTAL PROCEDURE

Samples were fabricated using an ultrahigh vacuum magnetron sputtering method. FePd films with the following two stacking structures were fabricated:

Series A: MgO (001) sub./Cr (34 nm)/Pd (17 nm)/$Fe_{50.5}Pd_{49.5}$ (16 nm)/MgO (2 nm)/Ta (5 nm).

Series B: $SrTiO_3$ (001) sub./ $Fe_{51.4}Pd_{48.6}$ (20 nm)/Ta (3 nm).

The MgO substrate is widely used for the fabrication of FePd films [14,18,22–24]. Cr and Pd are buffer materials used to relax lattice mismatch between the MgO substrate and FePd. On the other hand, lattice mismatch between FePd and $SrTiO_3$ is smaller than that between FePd and the MgO substrate, which indicates that the $SrTiO_3$ substrate is much more suitable for the fabrication of FePd thin films.

Film thicknesses and the composition of FePd for Series A were evaluated using Rutherford backscattering spectroscopy. The composition of FePd for Series B was evaluated using inductively coupled plasma atomic emission spectroscopy. FePd films were deposited during substrate heating with a substrate temperature T_s and annealed at an annealing temperature T_a.

The crystal structure and $L1_0$ order parameter were evaluated using X-ray diffraction (XRD). Both out-of-plane and in-plane XRD spectra were measured. Magnetic properties were characterized using a vibrating sample magnetometer (VSM). Both out-of-plane and in-plane magnetization curves were measured using VSM. Surface morphology was measured using atomic force microscopy (AFM). Magnetization dynamics was detected using TRMOKE. The wavelength, pulse repetition, and pulse width employed in the TRMOKE measurement were 800 nm, 1 kHz, and approximately 200 fs, respectively. An external magnetic field of 20 kOe with an arbitrary field angle can be applied in TRMOKE measurement.

III. RESULTS AND DISCUSSION

A. Crystal structure and surface morphology

Figure 1(a) shows typical out-of-plane XRD spectra for FePd films. The peaks at approximately 24° and 49° correspond to FePd (001) and FePd (002) peaks, which are

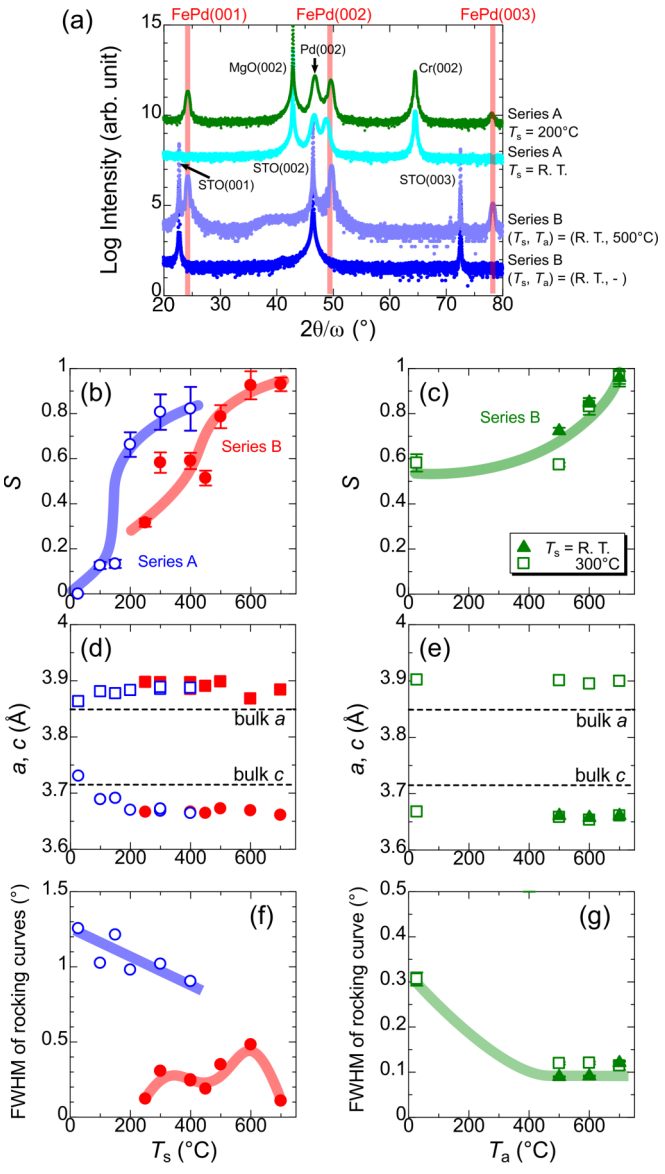

FIG. 1. (a) XRD $2\theta - \omega$ patterns for FePd films with different samples. (b) $L1_0$ order parameter S as a function of substrate temperature T_s for two different series. (c) S as a function of T_a for FePd film with Series B. Lattice constants a and c as a function of (d) T_s and (e) T_a. Full-width at half-maximum value of rocking curves for FePd (002) peaks as a function of (f) T_s and (g) T_a. Solid curves are guides to the eye. One can find data of Fig. 1(a) in the author's paper [19] and Figs. 1(a) and 1(b) in the author's paper [20].

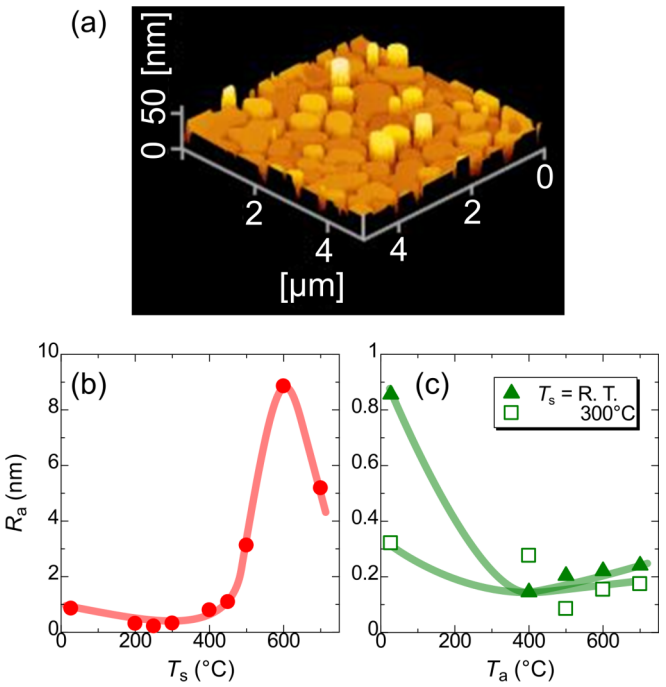

FIG. 2. (a) Surface morphology of FePd films for Series B with $T_s = 700\,^{\circ}\mathrm{C}$. Average surface roughness R_a of FePd films for Series B are plotted as a function of (b) T_s and (c) T_a. Solid curves in (b) and (c) are guides to the eye.

superlattice and fundamental peaks, respectively. The $L1_0$ order parameter S can be evaluated using the intensity ratio between FePd (001) and (002). S was calculated using the following formula: $S^2 = [I(001)/I(002)]/[I_{\mathrm{cal}}(001)/I_{\mathrm{cal}}(002)]$, where I and I_{cal} are the measured integrated intensity and the calculated intensity, respectively. Calculated intensity ratio was obtained using the following formula: $I_{\mathrm{cal}}(001)/I_{\mathrm{cal}}(002) = |F_{001}|^2 L_{001} A_{001}/|F_{002}|^2 L_{002} A_{002}$, where F, L, and A are the structural factor, Lorentz factor, and absorption factor, respectively. Figures 1(b) and 1(c) show S as a function of T_s and T_a. The results confirmed that S was increased with T_s and T_a. Lattice constant a and c values were evaluated using the peak positions of (110) and (002), respectively. The evaluated lattice constants as a function of T_s and T_a are shown in Figs. 1(d) and 1(e). The bulk values of a and c are taken from Ref. [3] and shown as broken lines. The a (c) constant evaluated for FePd films was larger (smaller) than that of bulk values, which may be attributed to the larger lattice constant a of the substrate and buffer layers. Figures 1(f) and 1(g) show the full-width at half-maximum (FWHM) of rocking curves evaluated for the FePd (002) peak as a function of T_s and T_a. The FWHM of rocking curves corresponds to the magnitude of the crystal axis dispersion. The FWHM of rocking curves for FePd film deposited on a $SrTiO_3$ substrate (Series B) was found to be smaller than that deposited on the MgO substrate (Series A).

Figure 2(a) shows the surface morphology measured using AFM of the FePd films for Series B with $T_s = 700\,^{\circ}\mathrm{C}$. Island growth in the film was observed for films deposited with T_s above $500\,^{\circ}\mathrm{C}$. Figures 2(c) and 2(d) show the average surface roughness R_a for FePd films with Series B as a function of T_s and T_a. A rough surface was observed for films deposited with large T_s, as shown in Fig. 2(b), whereas a smooth surface was obtained for films with low T_s and large T_a, as shown in Fig. 2(c).

B. Magnetic properties

Figure 3(a) shows magnetization curves for perpendicular and in-plane directions measured using VSM for FePd films with different series. Whereas FePd films deposited at room temperature (RT) showed in-plane magnetic anisotropy, films fabricated with large values of T_s and T_a exhibited PMA. Figures 3(b) and 3(c) show saturation magnetization M_s for FePd films fabricated under various conditions. The broken line represents a bulk value of 1100 emu/cm^3. M_s values for FePd films were close to those of bulk values and did not strongly depend on T_s and T_a. Figures 3(d) and 3(e) show K_u values for FePd films as a function of T_s and T_a. K_u values were found to be increased with increasing T_s and T_a, which may be a consequence of increasing S [see Figs. 1(f) and 1(g)]. Large coercivity, i.e., over 10 kOe, was observed for Series B for $T_s = 700\,^{\circ}\mathrm{C}$, which may be attributed to island growth on the film [see Fig. 2(a)].

C. Laser-induced magnetization dynamics and damping

Figure 4(a) shows a schematic illustration of the measurement configuration. Field angle θ_H and magnetization angle θ are defined as angles between the film normal and the external magnetic field and the magnetization, respectively. Figure 4(b) shows the TRMOKE signals obtained for FePd films deposited on a $SrTiO_3$ substrate with $T_a = 500\,^{\circ}\mathrm{C}$. The θ_H dependence of the TRMOKE signal at a fixed external magnetic field of 20 kOe was measured. Each TRMOKE signal was fitted by a damped sinusoidal function with exponential recovery of the background signal as

$$F(t) = A + B\exp(-\nu t) + \mathrm{amp}\,\exp\left(-\frac{t}{\tau}\right)\sin(2\pi f t + \phi), \tag{2}$$

where A, B, and ν are the signal offset, magnitude of the exponentially decayed background, and recovery rate of the background signal, respectively, amp, f, τ, and ϕ are the amplitude, frequency, relaxation time, and initial phase of the magnetization precession, respectively. The solid curves in Fig. 4(b) are results fitted using Eq. (2).

Figure 4(c) shows the frequency of magnetization precession obtained when the fit is plotted as a function of θ_H. The precession frequency f decreased with increasing θ_H. To explain the θ_H dependence of f and τ values, an analytical formula of f and τ was calculated using the LLG equation. One can calculate f_{LLG} and $1/\tau_{\mathrm{LLG}}$ from the linearized LLG equation [Eq. (1)] as follows:

$$f_{\mathrm{LLG}} = \frac{\gamma}{2\pi}\sqrt{H_{XX}H_{YY}}, \tag{3}$$

$$\frac{1}{\tau_{\mathrm{LLG}}} = \frac{1}{2}\alpha\gamma(H_{XX} + H_{YY}). \tag{4}$$

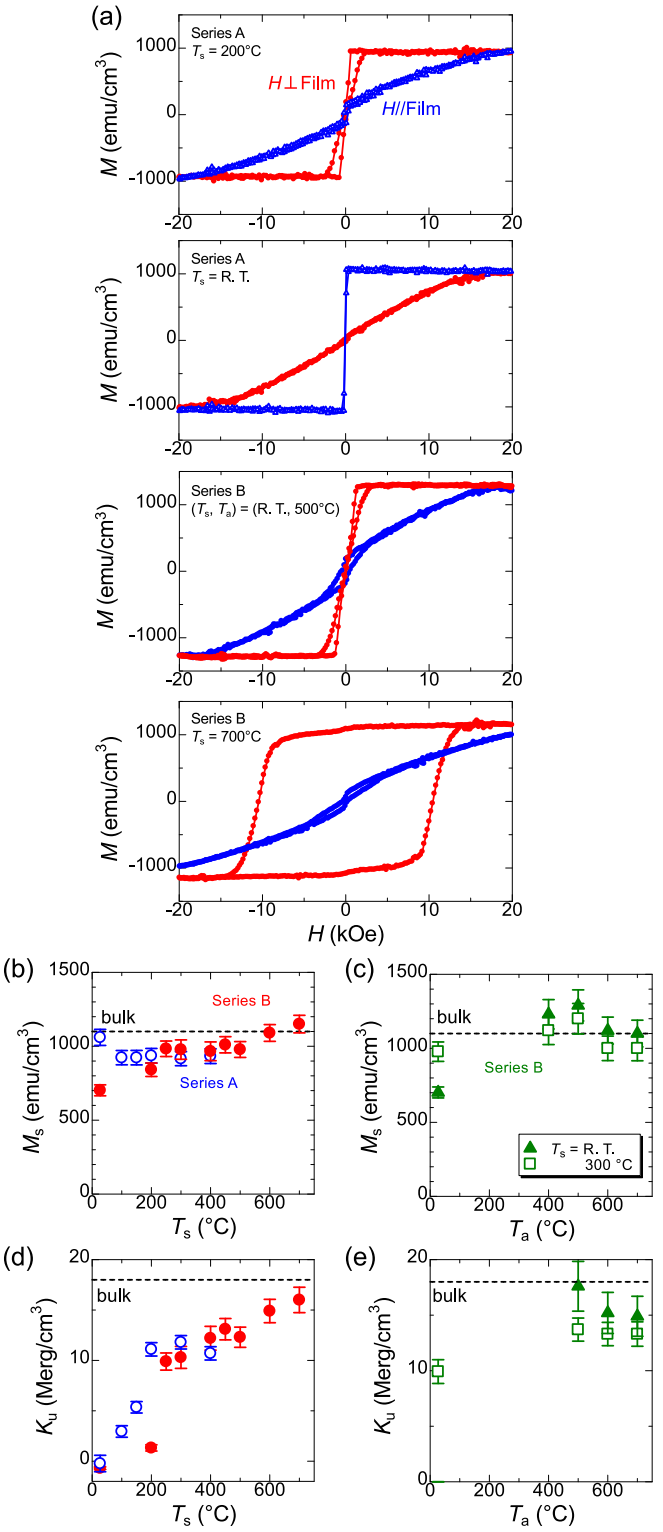

FIG. 3. (a) Magnetization curves measured using VSM for FePd films with different samples. (b) Saturation magnetization M_s as a function of T_s for FePd films with two different series. (c) M_s as a function of T_a for FePd films with Series B. Uniaxial perpendicular magnetic anisotropy constant K_u are plotted as a function of (d) T_s and (e) T_a. Dashed lines in (b)–(e) indicate the bulk values. One can find data of Fig. 2(b) in the author's paper [19] and Figs. 2(a)–2(c) in the author's paper [20].

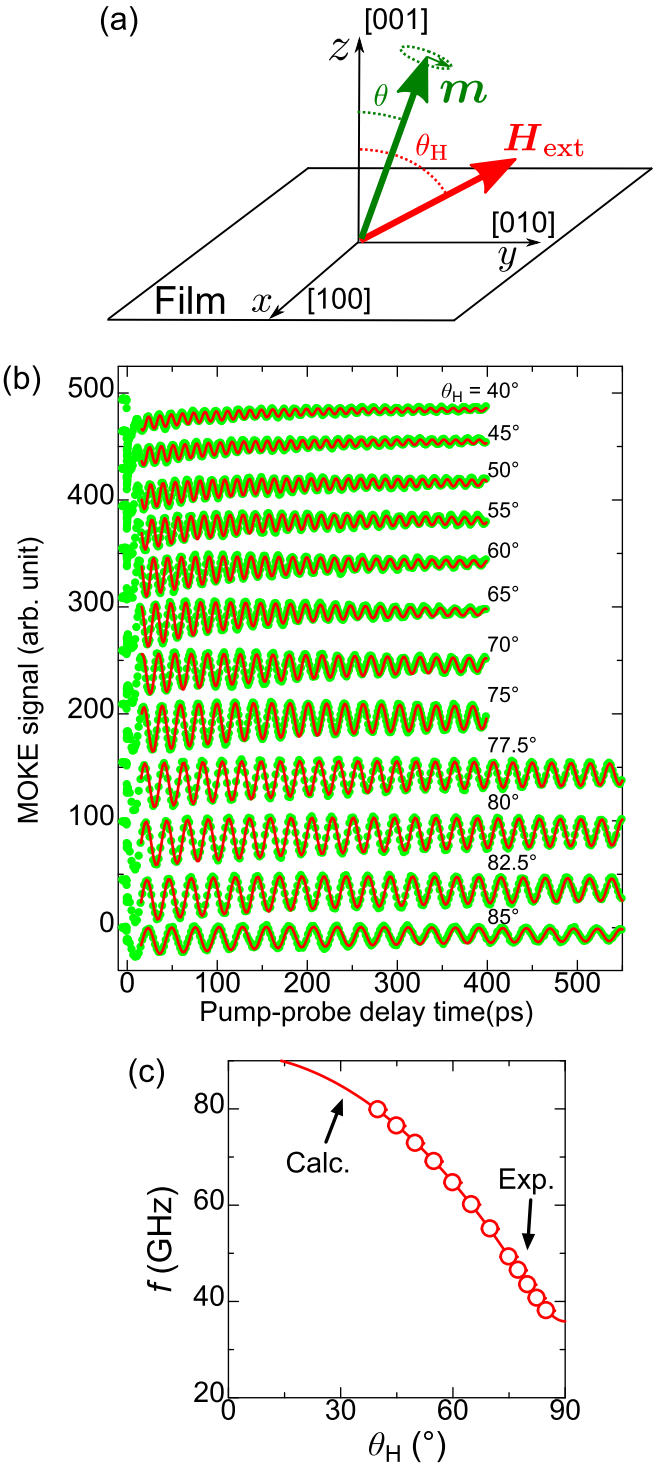

FIG. 4. (a) Coordinate system to describe the geometry of external magnetic fields and magnetization direction. (b) TRMOKE signals measured using different field angles θ_H at a fixed external field of 20 kOe for FePd film with perpendicular magnetic anisotropy. Solid curves in the figure are fitting results. (c) Precession frequency f as a function of θ_H. The solid curve in (c) represents a theoretical calculation.

Here, γ is defined as $\gamma = g\mu_B/\hbar$, where g, μ_B, and $\hbar$ are g factor, Bohr magnetron, and Dirac constant, respectively. H_{XX}

TABLE I. Evaluated parameters for FePd films for different samples. RT denotes room temperature. - means that no annealing was performed.

Series	(T_s, T_a)	S	M_s (emu/cm^3)	K_u (Merg/cm^3)	g factor	α
A	(RT, -)	0	1060 ± 54	0.2 ± 0.8	2.05	0.0067 ± 0.0003
A	(100 °C, -)	0.13	923 ± 48	3.0 ± 0.6	2.12	0.0072 ± 0.0005
A	(150 °C, -)	0.13	923 ± 49	5.4 ± 0.6	2.12	0.0063 ± 0.0005
A	(200 °C, -)	0.66	936 ± 49	11.1 ± 0.7	2.11	0.0022 ± 0.0004
A	(300 °C., -)	0.81	916 ± 48	11.8 ± 0.7	2.19	0.0029 ± 0.0021
A	(400 °C, -)	0.82	933 ± 50	10.7 ± 0.7	2.13	0.0058 ± 0.0017
B	(RT, -)		779 ± 63	−0.1 ± 0.3	2.14	0.0084 ± 0.0003
B	(RT, 500 °C)	0.72	1286 ± 105	18.3 ± 2.3	2.04	0.0037 ± 0.0015
B	(RT, 600 °C)	0.85	1123 ± 91	15.0 ± 1.9	2.07	0.0060 ± 0.0033
B	(RT, 700 °C)	0.96	1103 ± 90	13.8 ± 1.8	2.08	0.0164 ± 0.0037
B	(300 °C, 500 °C)	0.57	1200 ± 103	13.4 ± 1.0	2.03	0.0066 ± 0.0023
B	(300 °C, 600 °C)	0.83	1000 ± 84	13.5 ± 1.1	2.08	0.0073 ± 0.0025
B	(300 °C, 700 °C)	0.97	1000 ± 83	14.5 ± 1.1	2.04	0.0061 ± 0.0027
B	(700 °C, -)	0.93	1150 ± 59	16.0 ± 1.3	2.06	0.0197 ± 0.0037

and H_{YY} are given by

$$H_{XX} = H_{\rm ext}\cos(\theta - \theta_H) + H_k^{\rm eff}\cos^2\theta - H_{k2}\cos^4\theta, \quad (5)$$

$$H_{YY} = H_{\rm ext}\cos(\theta - \theta_H) + H_k^{\rm eff}\cos 2\theta - \tfrac{1}{2}H_{k2}(\cos 2\theta + \cos 4\theta), \quad (6)$$

where $H_{\rm ext}$, $H_k^{\rm eff}$, and H_{k2} are an external magnetic field, an effective PMA field, and a second-order PMA field, respectively. $H_k^{\rm eff}$ and H_{k2} are given by $H_k^{\rm eff} = 2K_u/M_s - 4\pi M_s + 4K_{u2}/M_s$ and $H_{k2} = 4K_{u2}/M_s$, respectively, where K_{u2} is a second-order crystalline uniaxial PMA constant. θ can be calculated using a minimum energy condition as

$$H_{\rm ext}\sin(\theta_H - \theta) - \tfrac{1}{2}H_k^{\rm eff}\sin 2\theta + \tfrac{1}{2}H_{k2}\sin 2\theta\cos^2\theta = 0. \quad (7)$$

The solid curve in Fig. 4(c) indicates the result calculated using Eq. (3). f values obtained from the experiment were accurately fitted by Eq. (3), and then, g and $H_k^{\rm eff}$ values were evaluated. Evaluated g values are listed in Table I. The K_u values shown in Fig. 3(d) and 3(e) were calculated using M_s and $H_k^{\rm eff}$, which were evaluated using the following relation: $K_u = M_s H_k^{\rm eff}/2 + 2\pi M_s^2 - M_s H_{k2}/2$. The evaluated K_u values are listed in Table I and discussed in Section III D.

Figure 5 shows the inverse of lifetime $1/\tau$ as a function of θ_H for different samples. The behavior of the θ_H dependence of $1/\tau$ is different for different samples. Figure 5(a) shows $1/\tau$ values obtained for Series A with T_s = RT, which exhibits in-plane magnetic anisotropy. The solid curve in Fig. 5(a) is the calculated result when using Eq. (4). Experimental $1/\tau$ values were well reproduced by Eq. (4) with $\alpha = 0.0067$. Figures 5(b)–5(f) show the $1/\tau$ responses obtained for Series A with T_s = 200 °C, Series B with (T_s, T_a) = (RT, 500 °C), (300 °C, 500 °C), (300 °C, 700 °C), and (700 °C, -) (- denotes no annealing was performed), all of which exhibited PMA. However, in the case of films with PMA, the θ_H dependence of $1/\tau$ values cannot be reproduced using the LLG equation, as indicated by the black solid curves in the figure. To elucidate the θ_H dependence of $1/\tau$, extrinsic contributions such as the anisotropy distribution and two-magnon scattering were considered. The increase in $1/\tau$ caused by the magnitude distribution of PMA can be approximated using [21,25,26]

$$\frac{1}{\tau^{H_k}} = \frac{1}{2}\left|\frac{d\omega_0}{dH_k^{\rm eff}}\right|\Delta H_k^{\rm eff}, \quad (8)$$

where ω_0 and $\Delta H_k^{\rm eff}$ are the resonance frequency ($\omega_0 = 2\pi f_{\rm LLG}$) and a value related to the dispersion magnitude of $H_k^{\rm eff}$. The increase in $1/\tau$ due to the axis distribution can be approximated by [21]

$$\frac{1}{\tau^{\theta_H}} = \frac{1}{2}\left|\frac{d\omega_0}{d\theta_H}\right|\Delta\theta_H, \quad (9)$$

where $\Delta\theta_H$ is the dispersion magnitude of the field angle. Details of the contribution of crystal axis distribution are presented in Appendix A. The contribution of two-magnon scattering $1/\tau^{\rm 2mag}$ can be calculated by [27–31]

$$\frac{1}{\tau^{\rm 2mag}} = N_0\sum_{\boldsymbol{k}}\frac{C(\boldsymbol{k})}{\omega_0}{\rm Im}\left(\frac{1}{\omega_k^2 - \omega_0^2 + i\omega_0\delta\omega_k}\right), \quad (10)$$

where N_0, $C(\boldsymbol{k})$, ω_k, and $\delta\omega_k$ are the scattering intensity, correlation function, dispersion relation of spin wave, and wave-vector-dependent inverse lifetime, respectively. Details of the two-magnon scattering are presented in Appendix B. Typical calculated results of $1/\tau^{H_k}$, $1/\tau^{\theta_H}$, and $1/\tau^{\rm 2mag}$ are shown in Fig. 6(b). The θ_H dependence of $1/\tau$ is different from that in intrinsic LLG equations, as shown in Fig. 6(a). $1/\tau$ for Series A with T_s = 200 °C is explained by summation of $1/\tau_{\rm LLG}$ and $1/\tau^{\theta_H}$ [dashed green curves in Fig. 3(b)]. Films of Series A showed large FWHM of rocking curves [Fig. 1(f)], i.e., films of Series A have a broader crystal axis distribution, which will contribute to enhance $1/\tau^{\theta_H}$. On the other hand, $1/\tau$ for samples of Series B are explained by summation of $1/\tau_{\rm LLG}$, $1/\tau^{H_K}$, and $1/\tau^{\rm 2mag}$ [dashed green curves in Figs. 5(c)–5(f)]. The α values of each sample were evaluated by fitting using the summation of intrinsic and extrinsic contributions. Details regarding the inhomogeneous parameter obtained in the analysis are presented in Appendix C. Evaluated α values are listed in Table I and discussed in Sec. III D.

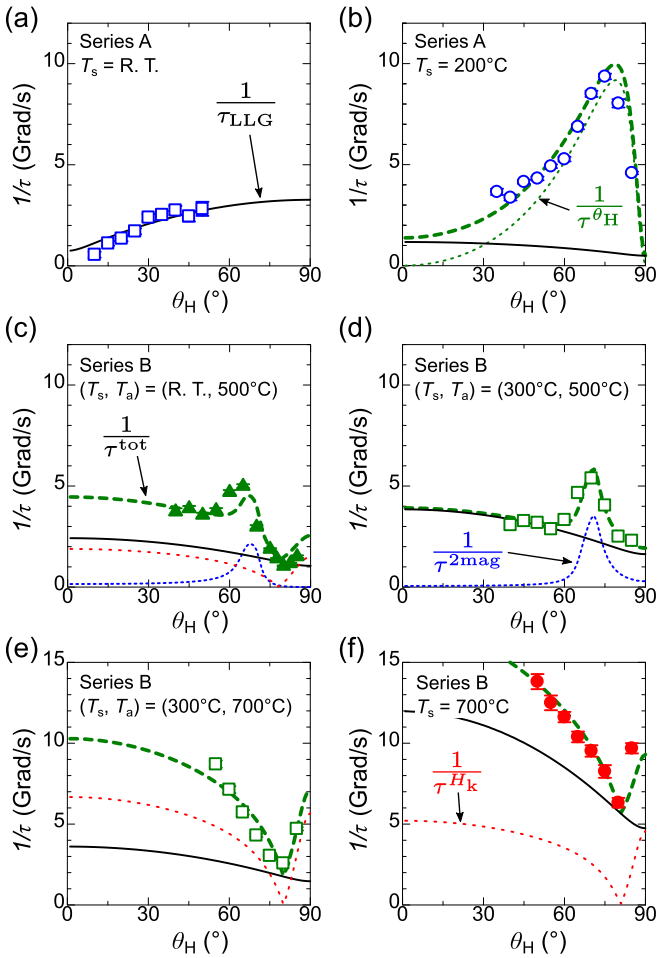

FIG. 5. Inverse of lifetime $1/\tau$ as a function of θ_H for FePd films for different samples. (a) and (b) correspond to Series A with T_s = RT and 200 °C, respectively. (c), (d), (e), and (f) correspond to Series B with (T_s, T_a) = (RT, 500 °C), (300 °C, 500 °C), (300 °C, 700 °C), and (700 °C, -), respectively. Solid curves in the figures indicate intrinsic contribution, stemming from LLG equation ($1/\tau_{LLG}$). Red, green, and blue dotted curves indicate contribution of anisotropy distribution ($1/\tau^{H_k}$), crystal axis distribution ($1/\tau^{\theta_H}$), and two-magnon scattering ($1/\tau^{2mag}$), respectively. Bold green broken curves are fitted results by using the summation of intrinsic and extrinsic contributions ($1/\tau^{tot}$).

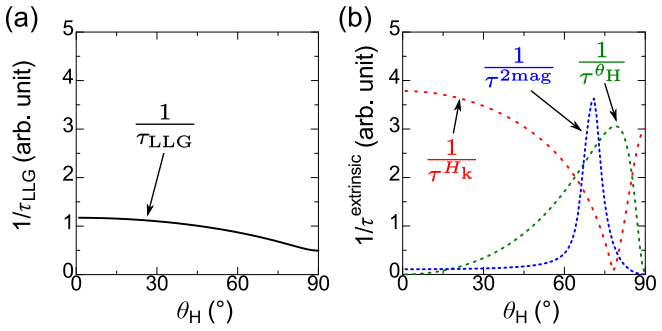

FIG. 6. Theoretical θ_H dependence of $1/\tau$. (a) $1/\tau_{LLG}$ intrinsic contribution, stemming from LLG equation, as a function of field angle θ_H. (b) $1/\tau^{H_k}$, $1/\tau^{\theta_H}$, and $1/\tau^{2mag}$, which are extrinsic contributions corresponding to the magnitude distribution of PMA, axis distribution, and two-magnon scattering as a function of θ_H.

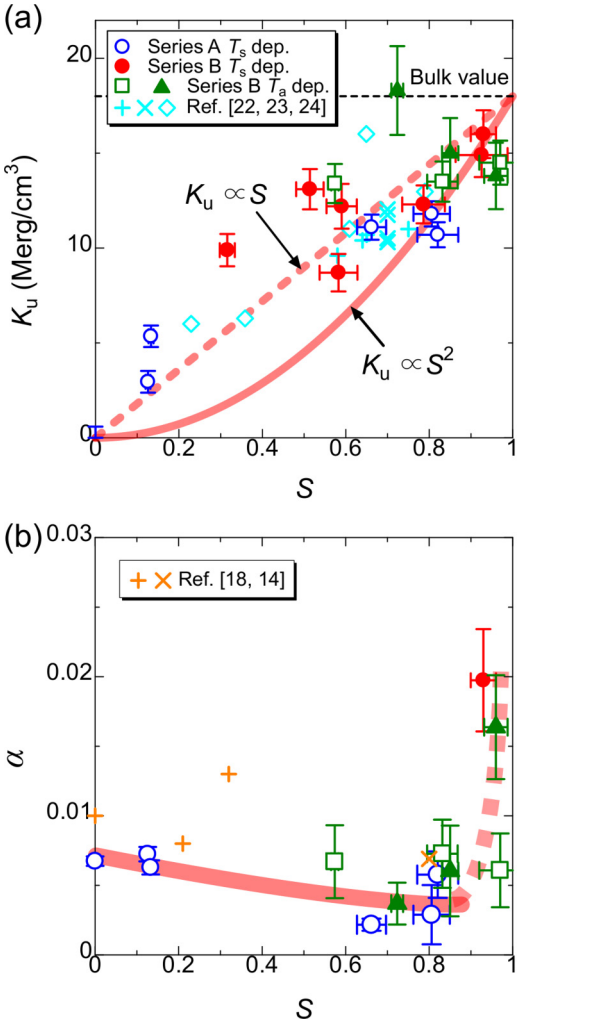

FIG. 7. (a) Uniaxial perpendicular magnetic anisotropy constant K_u as a function of the $L1_0$ order parameter S for FePd film for different samples. The broken line and solid curve indicate the linear relationship and the proposed theoretical relationship $K_u \propto S^2$. +, ×, and ◊ symbols in (a) represent values taken from Refs. [22–24], respectively. (b) Gilbert damping constant α as a function of S for FePd film for different samples. + and × symbols in (b) represent values taken from Refs. [14,18], respectively. Solid and dashed curves in (b) are a guide to the eye.

D. Order parameter dependence of K_u and α

Figure 7(a) shows the evaluated K_u values plotted as a function of S. The values taken from Refs. [22–24] are also plotted. The solid curve indicates a theoretical relationship, which is $K_u \propto S^2$ [7]. Experimental K_u values at approximately $S \sim 1$ were approximately 15 Merg/cm^3, which is close to the bulk value, whereas K_u did not follow the theoretical relation exactly. Linear relationship is also shown as broken line in Fig. 7(a), which seems to explain experimental data much more correctly than quadratic trend. One possible explanation of this linear relationship may be due to the mixed phase of low S and large S. Here, we assume that K_u value is average of the K_u at disordered phase ($S = 0$) and K_u at ordered phase ($S = 1$), i.e., $K_u = K_{u(S=0)}(1-x) + K_{u(S=1)}x$, where x indicates abundance ratio of the ordered phase. Since observed S is proportional to x, K_u will show linear relationship with S

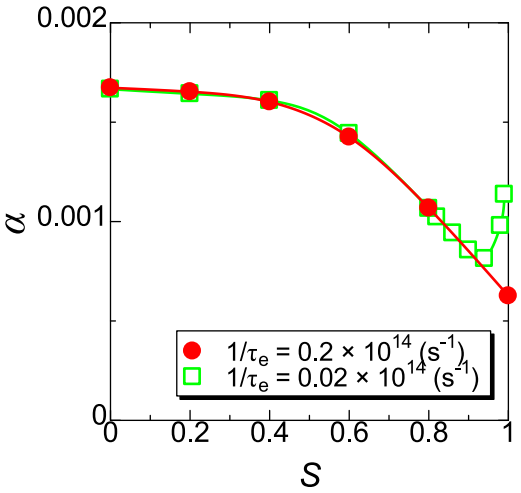

FIG. 8. Calculated α values for FePd with different $L1_0$ order parameters S. α values were calculated with two different electron scattering probabilities $1/\tau_e = 0.2 \times 10^{14}$ s^{-1} (filled bullet) and 0.02×10^{14} s^{-1} (open square).

in this assumption. Therefore, the existence of the mixed phase, which was not considered in the theory, may produce a discrepancy between experiment and theoretical relationship $K_u \propto S^2$.

Figure 7(b) shows the evaluated α values plotted as a function of S. The values reported in Refs. [14,18] are also plotted. α values in the low-S region are ~0.007 and decrease with increasing S. In addition, α had its minimum value ($\alpha = 0.002$–0.004) at approximately $S = 0.6$–0.8 and seemed to increase at approximately $S \sim 1$. To evaluate the S dependence of α, first-principles calculation of α was performed. Electronic structures were calculated using the tight-binding linear muffin-tin orbital method combined with coherent potential approximation to consider the disordered structure. α was calculated using the Kamberský torque correlation model [32–35]. Figure 8 shows the S dependence of calculated α values. α values were calculated with two different electron lifetimes τ_e. Although there is discrepancy in the magnitude of α between experiment and calculation, the trend of S dependence is discussed below. In the case of $1/\tau_e = 0.2 \times 10^{14}$ s^{-1}, calculated α values decreased with increasing S, which indicates that the interband contribution increases α with decreasing S. On the other hand, in the case of $1/\tau_e = 0.02 \times 10^{14}$ s^{-1}, α increased with increasing S at approximately $S\sim 1$, which is attributed to intraband contribution. This behavior was also calculated in the Fe-Pt alloy [32]. Therefore, a smaller $1/\tau_e$ value seems to explain the experimental trend. One can estimate $1/\tau_e$ from the electrical resistivity ρ using the following relation: $\rho = m/ne^2\tau_e$, where m, e, and n are the electron mass, electron charge, and electron density, respectively. The n value was calculated for FePd alloy using a valence electron number of 18. ρ value of 22.8 Ω m is used, which is taken from Ref. [36]. The $1/\tau_e$ value was estimated to be 1.15×10^{14} s^{-1}, which is much larger than that used in the calculation. The situation in which smaller $1/\tau_e$ values accurately reproduced experimental results was also observed in the temperature dependence of α in Fe_4N film [37].

Another possible reason for the enhancement of α is that the extrinsic contribution could not be completely removed in the analysis because accurate analysis of inhomogeneous contribution is thought to be quite difficult. If there is a large inhomogeneity in the film, magnetization dynamics will be complicated, which leads difficult to separate between intrinsic and extrinsic contributions completely. The α value for Series B with $T_s = 700\,^\circ$C which shows $S \sim 1$ might include extrinsic contribution because this sample showed island growth and large surface roughness. On the other hand, α values for Series B with (T_s, T_a) = (RT, 700 °C) and (300 °C, 700 °C) which showed continuous film and smooth roughness, and also showed $S \sim 1$ might not include extrinsic contribution very large. However, α values for their samples showed large value compared with that for the samples which showed $S = 0.6$–0.8 [Series B with (T_s, T_a) = (RT, 500 °C) and Series A with T_s = 200 °C and 300 °C]. Therefore, it can be said with certainty that α was increased with increasing S at approximately $S \sim 1$. Further detailed investigation of the S dependence of α should be performed by evaluating the τ_e value of the film and measuring the temperature dependence of α, which will be the subject of future research.

IV. CONCLUSION

We have systematically investigated the Gilbert damping constant α for $L1_0$-FePd films that have various S values using the TRMOKE technique. The θ_H dependence of TRMOKE signals were measured and analyzed. The θ_H dependence of $1/\tau$ values was explained by evaluating extrinsic contributions such as the anisotropy distribution and two-magnon scattering. K_u values for the films with $S \sim 1$ were found to be 15 Merg/cm^3, which is close to the value of the bulk. We found that α decreased with increasing S and that the minimum α value is 0.002–0.004 at approximately $S = 0.6$–0.8. The S dependence of α was evaluated using first-principles calculations. This investigation revealed that FePd alloy has both a large-K_u value of approximately 15 Merg/cm^3 and a small α value of less than 0.005, which is useful for low-power magnetization switching while maintaining a high thermal stability, as exploited in STT-MRAM applications.

ACKNOWLEDGMENTS

This work was supported by KAKENHI (Grant No. 24226001), a Tanaka Co. Ltd. grant, the New Energy and Industrial Technology Development Organization (NEDO) for Young Scientists (Grant No. 11B07018d), and the FIRST program. S.I. would like to thank the Japan Society for the Promotion of Science (JSPS) for their Grand-in-Aid for JSPS Fellows (Grant No. 28-7881). S.M. thanks to the Center for Spintronics Research Network.

APPENDIX A: DETAILS OF CRYSTAL AXIS DISTRIBUTION

In the main part of this text, Eq. (9) is used for the contribution of crystal axis distribution, which may be considerably simplified. Here, more accurate analysis of crystal axis distribution is presented. Distribution of perpendicular

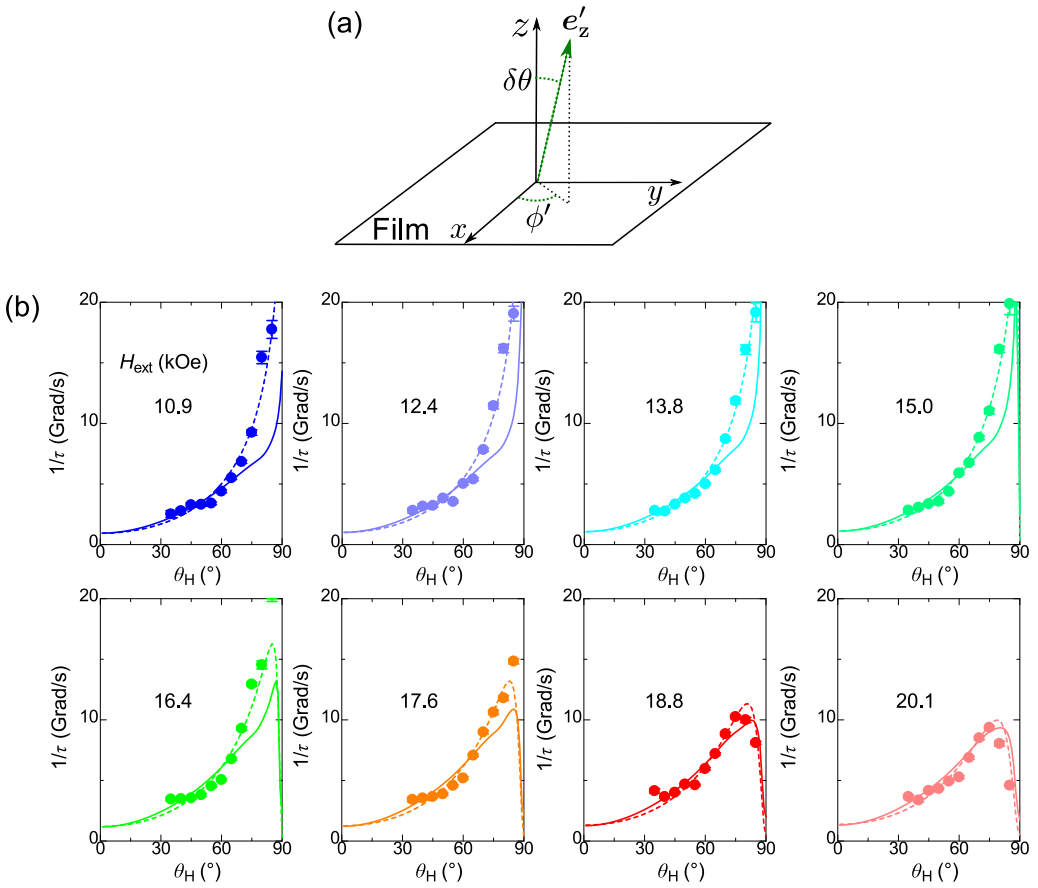

FIG. 9. (a) Coordinate system to describe crystal axis distribution. (b) Inverse of lifetime $1/\tau$ as a function of field angle θ_H measured at different external magnetic field H_{ext}. Sample corresponds to Series A with $T_s = 200\,^{\circ}$C. Solid and broken curves in the figures are simulated results by considering crystal axis distribution and the fitted results by using Eq. (9), respectively.

magnetic anisotropy energy can be calculated as

$$E_{\text{PMA}}(\boldsymbol{r}) = -K_u[\boldsymbol{m}\cdot\boldsymbol{e}'_z(\boldsymbol{r})]^2, \tag{A1}$$

where $E_{\text{PMA}}(\boldsymbol{r})$ and $\boldsymbol{e}'_z(\boldsymbol{r})$ are spatially dependent perpendicular magnetic anisotropy energy and spatially dependent crystal axis. Here, $\boldsymbol{e}'_z(\boldsymbol{r})$ can be calculated as

$$\boldsymbol{e}'_z(\boldsymbol{r}) = \sin\delta\theta(\boldsymbol{r})\cos\phi'(\boldsymbol{r})\boldsymbol{e}_x + \sin\delta\theta(\boldsymbol{r})\sin\phi'(\boldsymbol{r})\boldsymbol{e}_y + \cos\delta\theta(\boldsymbol{r})\boldsymbol{e}_z, \tag{A2}$$

where $\phi'(\boldsymbol{r})$ is assumed to be random distribution and $\delta\theta(\boldsymbol{r})$ was assumed to be Gaussian distribution. A coordinate system to describe crystal axis distribution is shown in Fig. 9(a). Superposition of magnetization precession for each crystal grain was calculated by

$$\overline{m_x}(t) = \frac{1}{N}\sum_{i,j} G(\delta\theta_i)m_x(\delta\theta_i,\phi'_j,t), \tag{A3}$$

where $G(\delta\theta_i)$ is Gaussian function and each m_x are calculated by LLG equation. Figure 9(b) shows $1/\tau$ as a function of θ_H measured at different H_{ext}. The sample corresponds to Series A with $T_s = 200\,^{\circ}$C. Solid curves in Fig. 9(b) are simulated results by using Eq. (A3) with $\alpha = 0.0022$ and $\sigma_{\delta\theta} = 1.0^{\circ}$, where $\sigma_{\delta\theta}$ is standard deviation of crystal axis. Experimental trends were well reproduced by Eq. (A3). Here, $\sigma_{\delta\theta}$ used is comparable to the broadening of rocking curves as shown in Fig. 1(f). In addition, fitted results by using Eq. (9) are also shown as broken curves in Fig. 9(b). The trends of crystal axis distribution are well reproduced by Eq. (9).

APPENDIX B: DETAILS OF TWO-MAGNON SCATTERING

A detailed description of the calculation of Eq. (10) is presented. The method of development of two-magnon scattering is taken primarily from Ref. [27]. Two-magnon scattering can be calculated from the self-energy of uniform magnetization precession [$\Sigma(0,\omega_0)$], which is given by [27]

$$\Sigma(0,\omega_0) = \sum_{\boldsymbol{k}} \frac{\gamma^2 N(0,\boldsymbol{k})}{\omega_k^2 - \omega_0^2 + i\omega_0\delta\omega_k}, \tag{B1}$$

where ω_k and $\delta\omega_k$ are the spin-wave dispersion relation and inverse lifetime of the spin wave, respectively. Here, $N(0,\boldsymbol{k})$ in the presence of a random inhomogeneous magnetic field h' can be calculated as follows [see Eq. (39) in Ref. [27] and Table I in Ref. [31]]:

$$N(0,\boldsymbol{k}) = \gamma^2\tfrac{1}{3}h'(0,\boldsymbol{k})^2(H_{XX}+H_{YY})^2, \tag{B2}$$

where h' is a random magnetic field. Here, the correlation function $C(\boldsymbol{k})$ is used to calculate the following equation:

$$|h'(0,\boldsymbol{k})|^2 = \langle h'^2\rangle C(\boldsymbol{k}), \tag{B3}$$

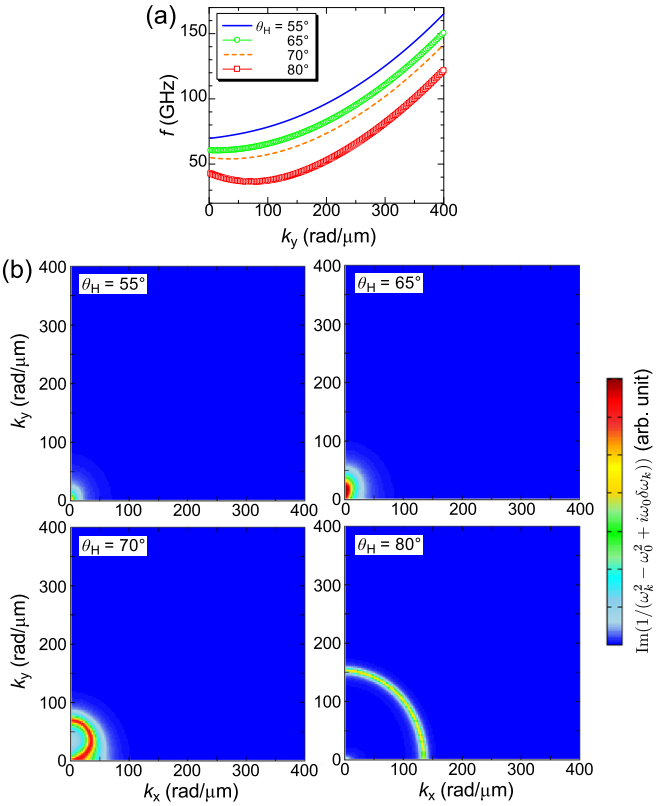

FIG. 10. (a) Spin-wave dispersion relation calculated for different values of θ_H. (b) Values related to the imaginary part of self-energy $\{\mathrm{Im}[1/(\omega_k^2 - \omega_0^2 + i\omega_0\delta\omega_k)]\}$ are plotted in a two-dimensional wave-vector space calculated for different values of θ_H.

where C($\boldsymbol{k}$) is given by [31]

$$C(\boldsymbol{k}) = \frac{2\pi\xi^2}{[1+(k\xi)^2]^{3/2}}. \tag{B4}$$

Here, ξ indicates the correlation length of the inhomogeneous magnetic field. Equation (10) can be derived using Eqs. (B1) and (B2) as follows:

$$\frac{1}{\tau^{2\mathrm{mag}}} = \frac{\mathrm{Im}\Sigma(0,\omega_0)}{\omega_0} = N_0 \sum_{\boldsymbol{k}} \frac{C(\boldsymbol{k})}{\omega_0} \mathrm{Im}\left(\frac{1}{\omega_k^2 - \omega_0^2 + i\omega_0\delta\omega_k}\right), \tag{B5}$$

where N_0 is defined as

$$N_0 = \frac{\gamma^4}{3}(H_{XX}+H_{YY})^2\langle h'^2\rangle. \tag{B6}$$

The spin-wave dispersion relation ω_k and the wave-vector-dependent inverse lifetime $\delta\omega_k$ were calculated using the formula [27,31,38]

$$\omega_k = \gamma\sqrt{H_{XX}(\boldsymbol{k})H_{YY}(\boldsymbol{k})}, \tag{B7}$$

$$\delta\omega_k = \alpha\gamma[H_{XX}(\boldsymbol{k}) + H_{YY}(\boldsymbol{k})]. \tag{B8}$$

$H_{XX}(\boldsymbol{k})$, $H_{YY}(\boldsymbol{k})$, and $H_{XY}(\boldsymbol{k})$ are given by

$$\begin{aligned} H_{XX}(\boldsymbol{k}) &= H_{\mathrm{ext}}\cos(\theta-\theta_H) + H_k\cos^2\theta \\ &\quad - 4\pi M_s\cos^2\theta + 4\pi M_s(1-N_k)(k_x/k)^2 \\ &\quad + (2A_{\mathrm{ex}}/M_s)k^2, \\ H_{YY}(\boldsymbol{k}) &= H_{\mathrm{ext}}\cos(\theta-\theta_H) + H_k\cos 2\theta \\ &\quad - 4\pi M_s\cos^2\theta + 4\pi M_s N_k\sin^2\theta \\ &\quad + 4\pi M_s(1-N_k)\cos^2\theta(k_y/k)^2 + (2A_{\mathrm{ex}}/M_s)k^2, \\ H_{XY}(\boldsymbol{k}) &= 4\pi M_s(1-N_k)(k_xk_y/k^2)\cos\theta, \end{aligned}$$

where H_k, A_{ex}, k_x, and k_y are the crystalline PMA field defined by $H_k = 2K_u/M_s$, exchange stiffness constant, x component of spin-wave wave vector, and y component of spin-wave wave vector, respectively. A_{ex} was set at 1.1×10^{-6} erg/cm, which is assumed to be the same as that of FePt [39,40]. N_k is a wave-number-dependent demagnetization factor, which is given by

$$N_k = \frac{1-\exp(-kd)}{kd},$$

where d is the film thickness.

Figure 10(a) shows ω_k plotted as a function of k_y for different values of θ_H. The slope of ω_k decreases with increasing θ_H. The slope around $k_y = 0$ becomes negative at approximately $\theta_H = 65°$–$70°$. Figure 10(b) shows $\mathrm{Im}[1/(\omega_k^2 - \omega_0^2 + i\omega_0\delta\omega_k)]$, which are values related to the intensity of two-magnon scattering [see Eq. (B5)], which are plotted in two-dimensional space calculated with different values of θ_H. The color intensity represents the states of the wave vector that satisfies $\omega_k = \omega_0$. There is strong peak at approximately $k \sim 0$ in the case of $\theta_H = 65°$ and $70°$; as a consequence, two-magnon scattering in this region of θ_H increased [see Fig. 6(b)].

ξ was used as a fitting parameter; however, the ξ values obtained from fitting were varied in the range of several tens of nm to several μm, and it seemed difficult to determine ξ. In addition, we also tried to consider Eq. (B2), which is the inhomogeneous magnetic field due to the PMA distribution. However, the θ_H dependence of $1/\tau^{2\mathrm{mag}}$ changes between the case where an inhomogeneous magnetic field is caused by the random magnetic field and the case where an inhomogeneous magnetic field is caused by distribution of PMA. We found that the random magnetic field explained the θ_H dependence of $1/\tau$, rather than the distribution of PMA.

APPENDIX C: PARAMETERS OF INHOMOGENEOUS MAGNETIC FIELD OBTAINED IN THE ANALYSIS

Here, the details of the parameters of inhomogeneous magnetic field obtained in the analysis are presented and discussed. In the case of the films of Series A, the θ_H dependence of $1/\tau$ is explained using summation of $1/\tau_{\mathrm{LLG}}$ [see Eq. (4)] and $1/\tau^{\theta_H}$ [see Eq. (9)] as shown in Fig. 5(b). In the case of films of Series B, the θ_H dependence of $1/\tau$ is explained using the summation of $1/\tau_{\mathrm{LLG}}$, $1/\tau^{H_k}$ [see Eq. (8)], and $1/\tau^{2\mathrm{mag}}$ [see Eq. (10)] as shown in Figs. 5(c)–5(f). The parameters that represent the inhomogeneity of the film obtained from fitting are shown in Table II. The $\Delta\theta_H$ parameter is found to be approximately

TABLE II. Evaluated parameters of inhomogeneous magnetic field obtained for FePd films with PMA. RT denotes room temperature. - means that no annealing was performed.

Series	(T_s, T_a)	$\Delta\theta_H$ (deg)[a]	$\Delta H_k^{\rm eff}$ (Oe)[b]	$\sqrt{\langle h'^2\rangle}$ (Oe)[c]	Remarks column
A	(200 °C, -)	8.9			
A	(300 °C., -)	8.4			
A	(400 °C, -)	10.1			
B	(RT, 500 °C)		270	170	
B	(RT, 600 °C)		480	140	
B	(RT, 700 °C)		2800		
B	(300 °C, 500 °C)		0	110	
B	(300 °C, 600 °C)		500	150	
B	(300 °C, 700 °C)		740		
B	(700 °C, -)		580		Island growth of the film[d]

[a]The parameter $\Delta\theta_H$ represents distribution of crystal axis, which is defined in Eq. (9).
[b]The parameter $\Delta H_k^{\rm eff}$ represents distribution of $H_k^{\rm eff}$, which is defined in Eq. (8).
[c]The parameter $\langle h'^2\rangle$ represents contribution of two-magnon scattering, which is defined in Eq. (B6).
[d]This sample showed island growth, which is confirmed by the AFM measurement shown in Fig. 2.

10 times larger than the FWHM of the rocking curve. This discrepancy may be due to the fact that $\Delta\theta_H$ does not reflect directly the distribution of crystal axis. On the other hand, the magnitude of the $1/\tau^{H_k}$ and $1/\tau^{\rm 2mag}$ were different for the samples of Series B. The magnitude of the inhomogeneous magnetic field and grain size determines which contribution is dominant between the anisotropy distribution and two-magnon scattering [41]. (The model of the anisotropy distribution is called the local resonance model in Ref. [41].) When the films have much more inhomogeneity, the contribution of $1/\tau^{H_k}$ becomes dominant. In the case of a film fabricated with the condition of $T_s = 700$ °C, which shows island growth and large surface roughness, the contribution of $1/\tau^{H_k}$ explains the θ_H dependence of $1/\tau$ [see Fig. 5(f)]. On the other hand, in the case of the film fabricated with the conditions of $(T_s, T_a) =$ (300 °C, 500 °C), which showed low surface roughness, the contribution of $1/\tau^{H_k}$ is suppressed and $1/\tau^{\rm 2mag}$ appeared [see Fig. 5(d)].

[1] T. Klemmer, D. Hoydick, H. Okumura, B. Zhang, and W. A. Soffa, Scr. Metall. Mater. **33**, 1793 (1995).
[2] D. Weller, A. Moser, L. Folks, M. E. Best, W. Lee, M. F. Toney, M. Schwickert, J. U. Thiele, and M. F. Doerner, IEEE Trans. Magn. **36**, 10 (2000).
[3] H. Shima, K. Oikawa, A. Fujita, K. Fukamichi, K. Ishida, and A. Sakuma, Phys. Rev. B **70**, 224408 (2004).
[4] W. F. Brown, Phys. Rev. **130**, 1677 (1963).
[5] J. C. Slonczewski, J. Magn. Magn. Mater. **159**, L1 (1996).
[6] P. Bruno, Phys. Rev. B **39**, 865 (1989).
[7] Y. Kota and A. Sakuma, J. Phys. Soc. Jpn. **81**, 084705 (2012).
[8] V. Kambersky, Can. J. Phys. **48**, 2906 (1970).
[9] V. Kambersky, Phys. Rev. B **76**, 134416 (2007).
[10] K. Gilmore, Y. U. Idzerda, and M. D. Stiles, J. Appl. Phys. **103**, 07D303 (2008).
[11] H. Ebert, S. Mankovsky, D. Kodderitzsch, and P. J. Kelly, Phys. Rev. Lett. **107**, 066603 (2011).
[12] S. M. Bhagat and P. Lubitz, Phys. Rev. B **10**, 179 (1974).
[13] X. Ma, L. Ma, P. He, H. B. Zhao, S. M. Zhou, and G. Lüpke, Phys. Rev. B **91**, 014438 (2015).
[14] P. He, X. Ma, J. W. Zhang, H. B. Zhao, G. Lupke, Z. Shi, and S. M. Zhou, Phys. Rev. Lett. **110**, 077203 (2013).
[15] J. Becker, O. Mosendz, D. Weller, A. Kirilyuk, J. C. Maan, P. C. M. Christianen, T. Rasing, and A. Kimel, Appl. Phys. Lett. **104**, 152412 (2014).
[16] S. Iihama, S. Mizukami, N. Inami, T. Hiratsuka, G. Kim, H. Naganuma, M. Oogane, T. Miyazaki, and Y. Ando, Jpn. J. Appl. Phys. **52**, 073002 (2013).
[17] S. Mizukami, S. Iihama, N. Inami, T. Hiratsuka, G. Kim, H. Naganuma, M. Oogane, and Y. Ando, Appl. Phys. Lett. **98**, 052501 (2011).
[18] T. Kawai, A. Itabashi, M. Ohtake, S. Takeda, and M. Futamoto, EPJ Web Conf. **75**, 02002 (2014).
[19] S. Iihama, A. Sakuma, H. Naganuma, M. Oogane, T. Miyazaki, S. Mizukami, and Y. Ando, Appl. Phys. Lett. **105**, 142403 (2014).
[20] S. Iihama, M. Khan, H. Naganuma, M. Oogane, T. Miyazaki, S. Mizukami, and Y. Ando, J. Magn. Soc. Jpn. **39**, 57 (2015).
[21] S. Mizukami, Y. Ando, and T. Miyazaki, Jpn. J. Appl. Phys. **40**, 580 (2001).
[22] J. R. Skuza, C. Clavero, K. Yang, B. Wincheski, and R. A. Lukaszew, IEEE Trans. Magn. **46**, 1886 (2010).
[23] J. Ko, T. Bae, and J. Hong, J. Appl. Phys. **112**, 113919 (2012).
[24] J. G. Ha, I. S. Chung, J. G. Kang, H. W. An, J. H. Koh, S. M. Koo, Y. H. Cho, S. Y. Park, M. H. Jung, and J. G. Kim, Phys. Status Solidi **204**, 4045 (2007).
[25] S. Iihama, S. Mizukami, H. Naganuma, M. Oogane, Y. Ando, and T. Miyazaki, Phys. Rev. B **89**, 174416 (2014).
[26] S. Mizukami, D. Watanabe, T. Kubota, X. Zhang, H. Naganuma, M. Oogane, Y. Ando, and T. Miyazaki, IEEE Trans. Magn. **47**, 3897 (2011).
[27] P. Landeros, R. E. Arias, and D. L. Mills, Phys. Rev. B **77**, 214405 (2008).
[28] R. Arias and D. L. Mills, Phys. Rev. B **60**, 7395 (1999).

[29] J. Lindner, I. Barsukov, C. Raeder, C. Hassel, O. Posth, R. Meckenstock, P. Landeros, and D. L. Mills, Phys. Rev. B **80**, 224421 (2009).
[30] J.-M. Beaujour, D. Ravelosona, I. Tudosa, E. E. Fullerton, and A. D. Kent, Phys. Rev. B **80**, 180415(R) (2009).
[31] R. D. McMichael and P. Krivosik, IEEE Trans. Magn. **40**, 2 (2004).
[32] A. Sakuma, J. Phys. Soc. Jpn. **81**, 084701 (2012).
[33] A. Sakuma, J. Phys. D: Appl. Phys. **48**, 164011 (2015).
[34] A. Sakuma, J. Magn. Soc. Jpn. **37**, 343 (2013).
[35] T. Qu and R. H. Victora, Appl. Phys. Lett. **106**, 072404 (2015).
[36] Y. Hsu, S. Jen, and L. Berger, J. Appl. Phys. **50**, 1907 (1979).
[37] S. Isogami, M. Tsunoda, M. Oogane, A. Sakuma, and M. Takahashi, J. Magn. Soc. Jpn. **38**, 162 (2014).
[38] S. Iihama, Y. Sasaki, A. Sugihara, A. Kamimaki, Y. Ando, and S. Mizukami, Phys. Rev. B **94**, 020401 (2016).
[39] S. Okamoto, N. Kikuchi, O. Kitakami, T. Miyazaki, Y. Shimada, and K. Fukamichi, Phys. Rev. B **66**, 024413 (2002).
[40] C. Antoniak, J. Lindner, K. Fauth, J. U. Thiele, J. Minar, S. Mankovsky, H. Ebert, H. Wende, and M. Farle, Phys. Rev. B **82**, 064403 (2010).
[41] R. D. McMichael, D. J. Twisselmann, and A. Kunz, Phys. Rev. Lett. **90**, 227601 (2003).